

# Large spin anomalous Hall effect in $L1_0$ -FePt: Symmetry and magnetization switching


Takeshi Seki,<sup>1,2,\*</sup> Satoshi Iihama,<sup>3</sup> Tomohiro Taniguchi,<sup>4</sup> and Koki Takanashi<sup>1,2</sup>

<sup>1</sup>*Institute for Materials Research, Tohoku University, Sendai 980-8577, Japan*

<sup>2</sup>*Center for Spintronics Research Network, Tohoku University, Sendai 980-8577, Japan*

<sup>3</sup>*WPI Advanced Institute for Materials Research, Tohoku University, Sendai 980-8577, Japan*

<sup>4</sup>*National Institute of Advanced Industrial Science and Technology (AIST), Spintronics Research Center, Tsukuba, 305-8568, Japan*

 (Received 10 May 2019; revised manuscript received 30 September 2019; published 18 October 2019)

The spin anomalous Hall effect (SAHE), generating spin angular momentum flow (spin current,  $\mathbf{J}_s$ ), in an  $L1_0$ -FePt ferromagnet was quantitatively evaluated by exploiting giant magnetoresistance devices composed of  $L1_0$ -FePt/Cu/Ni<sub>81</sub>Fe<sub>19</sub>. From the ferromagnetic resonance linewidth modulated by the charge current ( $\mathbf{J}_c$ ) injection, the spin anomalous Hall angle ( $\alpha_{\text{SAHE}}$ ) was obtained to be  $0.25 \pm 0.03$ . The evaluation of  $\alpha_{\text{SAHE}}$  at different configurations of  $\mathbf{J}_c$  and magnetization made it possible to discuss the symmetry of SAHE, giving the unambiguous evidence that SAHE is the source of  $\mathbf{J}_s$ . Thanks to the large  $\alpha_{\text{SAHE}}$ , the SAHE-induced magnetization switching was achieved.

DOI: [10.1103/PhysRevB.100.144427](https://doi.org/10.1103/PhysRevB.100.144427)

## I. INTRODUCTION

Highly efficient conversion from charge current ( $\mathbf{J}_c$ ) to spin current ( $\mathbf{J}_s$ ), which is the spin angular momentum flow, and vice versa is the key for spintronics to enhance device performance and to provide multifunctionalities. The most promising way to convert from  $\mathbf{J}_c$  to  $\mathbf{J}_s$  is to exploit the spin Hall effect (SHE) [1,2]. SHE is a relativistic effect expressed as

$$\mathbf{J}_s = [\hbar/(2e)]\alpha_{\text{SH}}[\hat{\sigma} \times \mathbf{J}_c], \quad (1)$$

where  $\alpha_{\text{SH}}$  is the spin Hall angle,  $e$  ( $<0$ ) is the electric charge of an electron,  $\hbar$  is the reduced Planck constant, and  $\hat{\sigma}$  is the quantization axis of electron spin. Equation (1) means when  $\mathbf{J}_c$  flows in a nonmagnet (NM), up- and down-spin electrons are scattered in opposite directions, resulting in the pure  $\mathbf{J}_s$  flow (i.e.,  $\mathbf{J}_s$  flow without net charge current flow) in the transverse direction to  $\mathbf{J}_c$ . The experimental studies on SHE were first done in nonmagnetic semiconductors [3,4] followed by the investigation of SHE in nonmagnetic metals [5], in which the NM with the large spin orbit coupling parameter is the key for observing the SHE.

As in the case of SHE in a NM, a ferromagnet (FM) is expected to exhibit charge-spin conversion [6]. In the early studies, the conversion from  $\mathbf{J}_s$  to  $\mathbf{J}_c$  in FM was reported [7–9]. After that, in 2015, the concept of spin anomalous Hall effect (SAHE) was proposed theoretically [10], and it was predicted that the anomalous Hall effect (AHE) also generates  $\mathbf{J}_s$ . More recently, several experimental works have reported the generation and detection of  $\mathbf{J}_s$  in the FMs [11–16]. The most apparent difference between SHE in NMs and SAHE in FMs is that due to the AHE the charge current appears in the transverse direction ( $\mathbf{J}_c^{\text{AHE}}$ ) [17] in the case of SAHE.  $\mathbf{J}_c^{\text{AHE}}$  is

defined as

$$\mathbf{J}_c^{\text{AHE}} = \alpha_{\text{AH}}[\hat{p} \times \mathbf{J}_c], \quad (2)$$

where  $\alpha_{\text{AH}}$  is the anomalous Hall angle, and  $\hat{p}$  is the quantization axis of local spin in the FM. According to the theory of SAHE [10], transverse  $\mathbf{J}_c^{\text{AHE}}$  is spin polarized by a factor  $\zeta$  that refers to the polarization of AHE. Although this  $\mathbf{J}_c^{\text{AHE}}$  gives rise to  $-\mathbf{J}_c^{\text{AHE}}$  under an open circuit condition,  $-\mathbf{J}_c^{\text{AHE}}$  is spin polarized by a factor  $\beta$  representing the spin polarization factor in the longitudinal  $\mathbf{J}_c$  flow. Consequently,  $\mathbf{J}_s$  originating from SAHE can be written as [10]

$$\mathbf{J}_s^{\text{SAHE}} = [\hbar/(2e)](\zeta - \beta)\alpha_{\text{AH}}[\hat{p} \times \mathbf{J}_c], \quad (3)$$

where  $(\zeta - \beta)\alpha_{\text{AH}}$  corresponds to spin anomalous Hall angle ( $\alpha_{\text{SAHE}}$ ). Equation (3) means that  $\mathbf{J}_s^{\text{SAHE}}$  depends on  $\hat{p}$ , i.e., magnetization ( $\mathbf{M}$ ). If  $\hat{p}$  is parallel to  $\mathbf{J}_c$ ,  $\mathbf{J}_s^{\text{SAHE}}$  becomes zero.

In contrast to the reports on SAHE [11–15], the recent studies have found the various phenomena differing from SAHE. For example, Tian and co-workers reported the  $M$ -independent conversion from  $\mathbf{J}_s$  to  $\mathbf{J}_c$  in a FM [18], which is similar to the inverse SHE in a NM. In Refs. [19,20], it was reported that the interface scattering leads to another spin polarization of electrons and the resultant spin orbit torques with symmetries different from that of SAHE. Therefore, in order to identify SAHE, it is necessary to eliminate the other effects. Another important issue concerning SAHE is its low conversion efficiency. SAHE has benefits that SHE does not have, e.g., the ability to reorient the antidamping torque along  $\hat{p}$ . If a FM layer exhibits the large SAHE and has magnetization tilted to the perpendicular direction to the film plane, the large SAHE can be used for the field-free magnetization switching of a perpendicularly magnetized free layer [10]. A FM exhibiting large  $\alpha_{\text{SAHE}}$  is thus the first essential for realizing the SAHE-based spintronic device.

This study focuses on ferromagnetic  $L1_0$ -FePt because large AHE has been reported for the  $L1_0$ -FePt [21]. The

\*go-sai@imr.tohoku.ac.jp

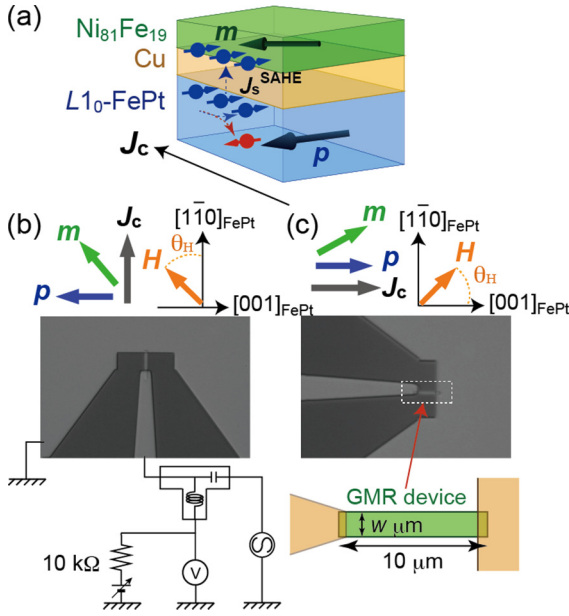


FIG. 1. (a) Schematic illustration of SAHE in  $L1_0$ -FePt (30 nm)|Cu (3 nm)|Py (2 nm), where  $\mathbf{p}$  and  $\mathbf{m}$  are the unit vectors of  $L1_0$ -FePt and Py magnetizations, respectively.  $\mathbf{J}_c$  denotes the charge current flow, and  $\mathbf{J}_s^{\text{SAHE}}$  denotes the spin current originating from SAHE. (b) Optical microscope images of devices with orthogonal configuration and (c) parallel configuration together with the relationship between  $\mathbf{p}$ ,  $\mathbf{m}$ ,  $\mathbf{J}_c$ , and external magnetic field ( $\mathbf{H}_{\text{ext}}$ ).  $\theta_H$  was defined as the angle from  $\mathbf{J}_c$ . The setup for measuring FMR and the enlarged illustration of the GMR device are also depicted.

magnitude of SAHE in the  $L1_0$ -FePt was quantitatively evaluated, and the symmetry of SAHE was examined in order to distinguish the SAHE from the other effects. The large SAHE of  $L1_0$ -FePt was found, which made it possible to demonstrate the SAHE-induced magnetization switching. In order to evaluate  $\alpha_{\text{SAHE}}$  quantitatively, the ferromagnetic resonance (FMR) measurement was carried out for a giant magnetoresistance (GMR) device composed of  $L1_0$ -FePt|Cu|Ni<sub>81</sub>Fe<sub>19</sub> (permalloy: Py), in which  $L1_0$ -FePt has the in-plane uniaxial magnetic anisotropy. Figure 1(a) schematically illustrates the SAHE in the present GMR stack. The applied dc current (corresponding to  $\mathbf{J}_c$ ) flowing in the  $L1_0$ -FePt layer is converted into  $\mathbf{J}_s^{\text{SAHE}}$ , which interacts with  $\mathbf{M}$  of Py (whose unit vector is defined as  $\mathbf{m}$ ), resulting in the modification of the FMR linewidth due to the enhanced or reduced magnetization damping of Py. The key of this study is that the strong in-plane uniaxial magnetic anisotropy of  $L1_0$ -FePt enables us to utilize two different relative configurations of  $\mathbf{J}_c$  and  $\mathbf{M}$  of FePt (whose unit vector is defined as  $\mathbf{p}$ ). As shown in Fig. 1(a), the orthogonal configuration of  $\mathbf{J}_c \perp \mathbf{p}$  corresponds to the configuration for evaluating the SAHE. In the parallel configuration of  $\mathbf{J}_c \parallel \mathbf{p}$ , other possible effects such as SHE and the interface scattering effect can be identified, which will be discussed in Sec. III. Thus, two kinds of devices, which are the orthogonal- and parallel-configuration devices [Figs. 1(b) and 1(c)], were utilized in this study.

## II. EXPERIMENTAL PROCEDURE

Thin films with a stack of FePt (30)|Cu (3)|Py (2)|Al-O (10) (in nanometers) were grown on an SrTiO<sub>3</sub> (110) single crystal substrate. All the layers except FePt were grown at ambient temperature. The FePt layer was deposited on the SrTiO<sub>3</sub> substrate using an ultrahigh-vacuum magnetron sputtering system at 450 °C. After depositing the FePt layer, the sample was transferred to an ion beam sputtering (IBS) chamber. After cleaning the FePt surface by soft Ar ion milling, the Cu|Py|Al-O layers were deposited on the FePt layer employing the IBS. The crystal structure of the thin film was characterized using x-ray diffraction (XRD) with Cu  $K\alpha$  radiation. The alloy compositions of FePt and Py were determined to be Fe<sub>54</sub>Pt<sub>46</sub> and Ni<sub>81</sub>Fe<sub>19</sub>, respectively, by electron probe x-ray microanalysis. Magnetization of the thin film was measured at room temperature using a vibrating sample magnetometer.

Rectangular-shaped devices with orthogonal and parallel configurations were fabricated on an identical substrate [Figs. 1(b) and 1(c)]. The thin films were patterned into rectangular shapes through the use of electron beam lithography and Ar ion milling. Then, the Au|Cr contact pads with a coplanar waveguide (CPW) shape were formed. The length of the GMR device was fixed at 10  $\mu\text{m}$  while the width ( $w$ ) of the device was varied:  $w = 1$  or 4  $\mu\text{m}$ . For the FMR measurement, together with the dc current ( $I_{\text{dc}}$ ), the radiofrequency current ( $I_{\text{rf}}$ ) was applied to the device to generate an oscillating transverse magnetic field, which excited the FMR in the Py layer. The rf power of 5 dBm with the fixed  $f_0$  was applied to the signal line of the CPW from a signal generator. When the condition of FMR in the Py was satisfied at a certain external magnetic field ( $H_{\text{ext}}$ ), the device resistance [ $R(t)$ ] oscillated through the GMR effect. As a result, applied  $I_{\text{rf}}(t) [= I \cos(2\pi f_0 t)]$  and oscillating  $R(t) [\propto \cos(2\pi f_0 t)]$  generated a rectification dc voltage ( $V_{\text{dc}}$ ), which was detected by a lock-in amplifier. For the FMR measurement with the  $I_{\text{dc}}$  application, a sourcemeter was connected to the dc port of bias T.

## III. RESULTS AND DISCUSSION

### A. Structure and magnetic properties of GMR trilayer

The structure and magnetic properties of the GMR trilayer are first explained. Figures 2(a)–2(c) display XRD profiles for the  $L1_0$ -FePt|Cu|Py stack. The out-of-plane XRD profile [Fig. 2(a)] shows only 220 diffractions of FePt, Cu, and Py while in the in-plane XRD profile [Fig. 2(b)] only 00 $l$  diffractions of FePt, Cu, and Py are observed. These results indicate that all the layers were grown on the SrTiO<sub>3</sub> (110) substrate with (110) crystal orientation in the normal direction to the film plane. In the in-plane  $\phi$  scan for FePt 200 diffraction [Fig. 2(c)], the twofold rotational symmetry is observed. It is therefore found that the GMR trilayer was epitaxially grown with the relationship of  $(110)_{\text{SrTiO}_3} \parallel (110)_{\text{FePt}} \parallel (110)_{\text{Cu}} \parallel (110)_{\text{Py}}$ ,  $[001]_{\text{SrTiO}_3} \parallel [001]_{\text{FePt}} \parallel [001]_{\text{Cu}} \parallel [001]_{\text{Py}}$ . In addition, the FePt 001 and 003 superlattice peaks appearing in Fig. 2(b) indicate that the  $L1_0$ -ordered FePt was formed. The relationship between the crystal orientations of SrTiO<sub>3</sub> and  $L1_0$ -FePt is schematically illustrated in Fig. 2(d).

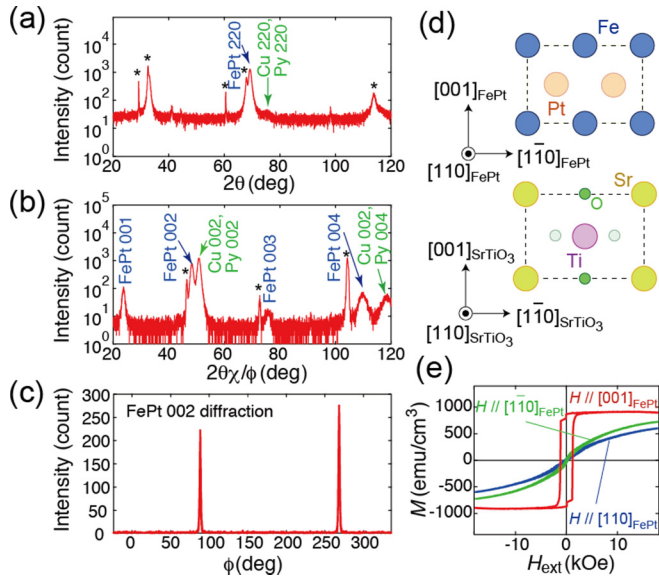


FIG. 2. (a) Out-of-plane and (b) in-plane x-ray diffraction profiles for the  $L1_0$ -FePt (30 nm)|Cu (3 nm)|Py (2 nm) stack. Asterisks denote the reflections from the  $\text{SrTiO}_3$  (110) substrate. (c) In-plane  $\phi$  scan for FePt 200 diffraction. (d) Illustration of the epitaxial relationship between the  $\text{SrTiO}_3$  (110) and  $L1_0$ -FePt (110) planes. (e) Magnetization curves with  $H_{\text{ext}}$  applied in the in-plane [001] (red line) direction, the in-plane  $[1\bar{1}0]$  direction (green line), and the out-of-plane  $[110]$  direction (blue line).

Figure 2(e) shows the magnetization curves with  $H_{\text{ext}}$  applied along the in-plane [001] direction, the in-plane  $[1\bar{1}0]$  direction, and the out-of-plane  $[110]$  direction. It is obvious that the  $L1_0$ -FePt layer has the strong in-plane uniaxial magnetic anisotropy in the in-plane [001] direction because of the high remanent magnetization in the [001] direction and the large saturation field in the  $[1\bar{1}0]$  direction. This uniaxial magnetic anisotropy comes from the magnetocrystalline anisotropy of  $L1_0$ -FePt, since the  $c$  axis, i.e., the [001] direction, is the

easy magnetization axis for  $L1_0$ -FePt. As in the case of the  $L1_0$ -FePt layer, the Py layer exhibits the non-negligible in-plane magnetic anisotropy in the [001] direction. Two-step behavior of magnetization switching is observed in the low  $H_{\text{ext}}$  region of the in-plane [001] magnetization curve. An important point is that a difference in the coercivities of the  $L1_0$ -FePt and Py layers is induced.

## B. FMR linewidth modulated by SAHE

Figure 3(a) shows current-in-plane (CIP) GMR curves for the orthogonal-configuration device with  $w = 4 \mu\text{m}$  at the magnetic field angles ( $\theta_H$ ), as defined in Fig. 1(b), of  $0^\circ$ ,  $15^\circ$ , and  $90^\circ$ . The MR curves measured at the other  $\theta_H$  are given in the Supplemental Material [22] (see, also, Refs. [23–27]). A perpendicular configuration between  $\mathbf{p}$  and  $\mathbf{m}$  is achieved for  $\theta_H = 0^\circ$  by increasing  $H_{\text{ext}}$ . On the other hand, a full GMR curve with the complete parallel and antiparallel alignments of  $\mathbf{p}$  and  $\mathbf{m}$  is obtained when  $H_{\text{ext}}$  is swept at  $\theta_H = 90^\circ$ . These MR curves indicate that  $\mathbf{m}$  is easily aligned along  $\mathbf{H}_{\text{ext}}$  while  $\mathbf{p}$  acts as a fixed polarizer, resulting in the orthogonal configuration between  $\mathbf{p}$  and  $\mathbf{J}_c$  as expected.

Figures 3(b) and 3(c) show FMR spectra for the orthogonal-configuration device at  $I_{\text{dc}} = 4 \text{ mA}$  and  $-4 \text{ mA}$ , respectively.  $\theta_H$  was set at  $-10^\circ$  and  $f_0$  was set at 4 GHz.  $V_{\text{dc}}$  appears due to the rectification effect through the CIP-GMR effect, and the resonance peak comes from the FMR of Py. The experimental spectra were fitted by Lorentzian and anti-Lorentzian functions together with a linear function to account for the slight linear change in the device resistance with  $H_{\text{ext}}$  (see the Supplemental Material [22] for details of fitting). One can see the clear variation in the spectral linewidth ( $\Delta H_{\text{Res}}$ ) between  $I_{\text{dc}} = 4 \text{ mA}$  and  $-4 \text{ mA}$ .  $\Delta H_{\text{Res}}$  versus  $I_{\text{dc}}$  for  $\theta_H = -10^\circ$  and  $15^\circ$  is plotted in Figs. 3(d) and 3(e), respectively. The linear variations in  $\Delta H_{\text{Res}}$  are observed, and the slope of the plots depends on  $\theta_H$ . It is noted that the odd-functional behavior of  $\Delta H_{\text{Res}}$  against  $I_{\text{dc}}$  is not explained

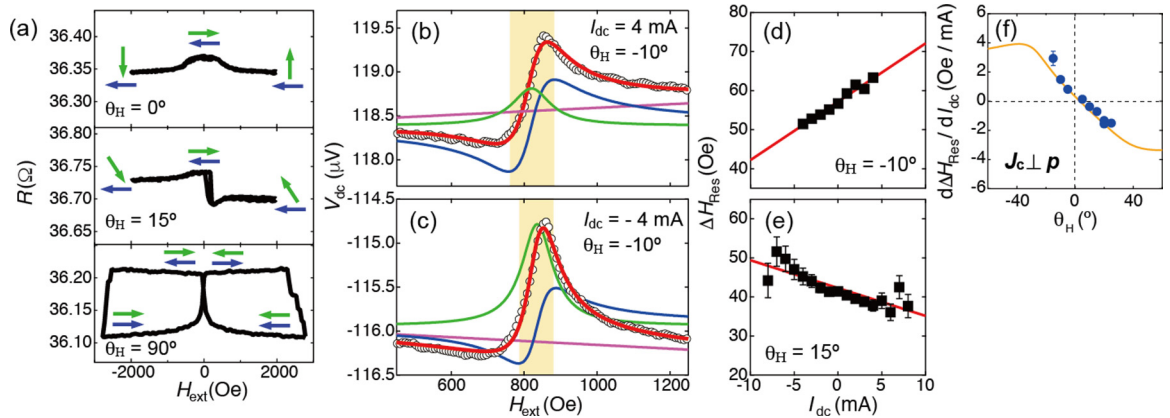


FIG. 3. (a) Magnetoresistance curves for the orthogonal-configuration device with  $w = 4 \mu\text{m}$  at  $\theta_H = 0^\circ$ ,  $15^\circ$ , and  $90^\circ$ . Blue and green arrows denote the  $L1_0$ -FePt ( $\mathbf{p}$ ) and Py magnetizations ( $\mathbf{m}$ ), respectively. (b) FMR spectra for the orthogonal-configuration device with  $w = 4 \mu\text{m}$  under the application of  $I_{\text{dc}} = 4 \text{ mA}$  and (c)  $-4 \text{ mA}$ .  $\theta_H$  was set to  $-10^\circ$  and  $f_0$  was 4 GHz. The experimental data (black open circles) were fitted by a function (red curves) composed of Lorentzian (green curves) and anti-Lorentzian (blue curves) together with the linear background (purple lines). The orange shaded areas are guides for the eye to see the linewidth modulation. (d)  $\Delta H_{\text{Res}}$  versus  $I_{\text{dc}}$  for  $\theta_H = -10^\circ$  and (e)  $15^\circ$  for the orthogonal-configuration device. (f)  $d\Delta H_{\text{Res}}/dI_{\text{dc}}$  as a function of  $\theta_H$  for the orthogonal-configuration device. The solid curve represents the fitting result obtained using Eq. (4).

by the spin-transfer torque (STT) of the GMR stack because the sign of STT, i.e., damping or antidamping, due to the CIP-GMR effect is not determined by the direction of  $I_{dc}$ . Figure 3(f) summarizes modulation linewidth,  $d\Delta H_{Res}/dI_{dc}$ , as a function of  $\theta_H$  for the orthogonal-configuration device. The experimental values of  $d\Delta H_{Res}/dI_{dc}$  were well fitted by the following equation:

$$\frac{d\Delta H_{Res}}{dI_{dc}} = \alpha_{SAH} \frac{\hbar}{e} \left( \frac{C^{FePt}}{wd^{FePt}} \right) \left[ \frac{2\pi f_0}{\gamma \cos(\varphi^{Py} - \theta_H)} \right] \times \left[ \frac{\sin \varphi^{Py}}{\mu_0 M_s^{Py} d^{Py} (H_{XX} + H_{YY})} \right], \quad (4)$$

where  $C^{FePt}$  is the shunt ratio of the current flowing in the  $L1_0$ -FePt layer to total  $I_{dc}$ ,  $\gamma$  is the gyromagnetic ratio,  $\mu_0$  is the permeability in vacuum,  $\varphi^{Py}$  is the angle of  $\mathbf{m}$  respective to  $\mathbf{J}_c$ ,  $M_s^{Py}$  is the saturation magnetization of Py, and  $H_{XX(YY)}$  represents the in-plane (out-of-plane) effective field for the Py layer.  $d^{FePt}$  and  $d^{Py}$  are the thicknesses of the  $L1_0$ -FePt and Py layers, respectively. We assumed that  $\mathbf{p}$  is pinned in the direction orthogonal to  $\mathbf{J}_c$ . The values of  $\gamma$ ,  $\varphi^{Py}$ ,  $M_s^{Py}$ , and  $H_{XX(YY)}$  were determined by the  $\theta_H$  dependence of the FMR spectra without the  $I_{dc}$  application (Supplemental Material [22]). In this study, we obtained  $\gamma = 2.11 \mu_B/\hbar$  and  $M_s^{Py} = 225 \text{ emu/cm}^3$ .  $C^{FePt}$  was calculated to be 0.315 in consideration of the parallel circuit with the resistivities ( $\rho$ ) of  $L1_0$ -FePt, Cu, and Py ( $\rho_{L1_0\text{-FePt}} = 93 \mu\Omega \text{ cm}$ ,  $\rho_{Cu} = 4.5 \mu\Omega \text{ cm}$ , and  $\rho_{Py} = 60 \mu\Omega \text{ cm}$ ). As a result,  $\alpha_{SAHE}$  for the orthogonal-configuration device is obtained to be  $0.25 \pm 0.03$ . This value of  $\alpha_{SAHE}$  is significantly larger than  $-0.14 \pm 0.05$  for CoFeB [13]. As introduced in Sec. I,  $\alpha_{SAHE}$  is given by  $(\zeta - \beta)\alpha_{AH}$ .  $\alpha_{AH}$  of FePt was evaluated to be 0.03 by measuring AHE (see the Supplemental Material [22] for the AHE curve). According to the previous transport experiments using  $L1_0$ -FePt [28],  $\beta$  is considered to be 0.4 at most. This means that large  $\zeta = 8.7$  is required in order to explain the large  $\alpha_{SAHE}$ . It is noted that the parameter  $\zeta$  is defined as a ratio of the spin current to the transverse charge current induced by AHE. Therefore, if the spin-up and spin-down electrons are scattered in the opposite directions,  $\zeta$  can be larger than 1. The parameter  $\zeta$  was introduced in Ref. [10] phenomenologically, and an evaluation of its value by, for example, first-principles calculation, has not been reported for the  $L1_0$ -FePt yet. Our result given above, however, suggests that even a FM with a small  $\alpha_{AH}$  can be a highly efficient  $\mathbf{J}_s$  source using the SAHE.

In order to exclude the possibility of self-induced spin torque in the Py layer and the interface effect at the Cu | Py interface as mechanisms for the FMR linewidth modulation, a control experiment was performed using a reference sample consisting of a Cu (3)|Py (2)|Al-O (10) (in nanometers) stack as schematically shown in Fig. 4(a). As shown in Fig. 4(b), the reference sample exhibits a clear resistance change due to the anisotropic magnetoresistance (AMR) effect. Figure 4(c) displays FMR spectra for the reference sample at various rf frequencies of  $H_{rf}$  without  $I_{dc}$  application.  $\theta_H$  was fixed at  $45^\circ$  because  $V_{dc}$  was maximum at  $\theta_H = 45^\circ$  in the AMR case.  $H_{Res}$  is increased with  $f$ . At  $\theta_H = 45^\circ$  and  $f = 7 \text{ GHz}$ , the effect of  $I_{dc}$  application on  $\Delta H_{Res}$  was examined as shown

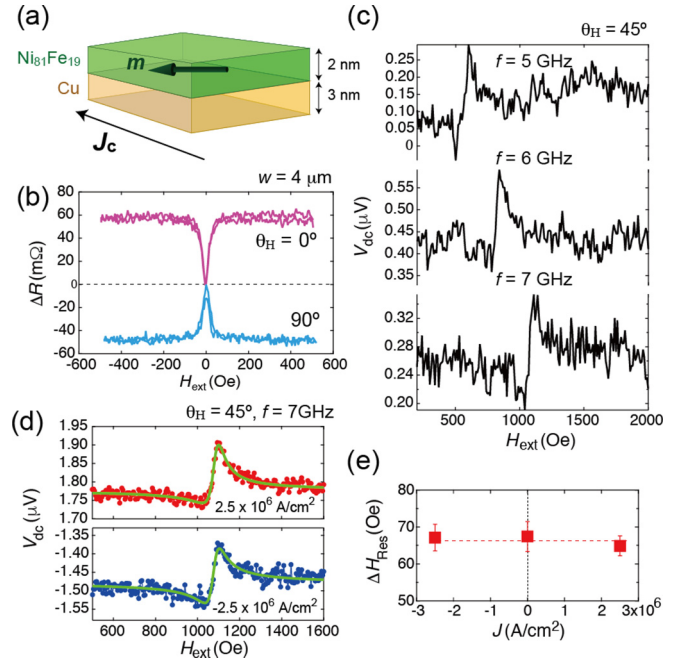


FIG. 4. Control experiment using a reference sample with a Cu|Py|Al-O stack. (a) Schematic illustration of the reference sample. (b) Anisotropic magnetoresistance (AMR) curves measured at  $\theta_H = 0^\circ$  and  $90^\circ$ . (c) FMR spectra at the  $H_{rf}$  frequencies of 5, 6, and 7 GHz without  $I_{dc}$  application.  $\theta_H$  was fixed at  $45^\circ$ . (d) FMR spectra measured under the  $I_{dc}$  application, where applied current density ( $J$ ) was set at  $\pm 2.5 \times 10^6 \text{ A/cm}^2$ . (e)  $\Delta H_{Res}$  as a function of  $J$ .

in Figs. 4(d) and 4(e). The reference sample shows no remarkable linewidth modulation even at the applied current density ( $J$ ) of  $2.5 \times 10^6 \text{ A/cm}^2$ . Since  $J = 2.5 \times 10^6 \text{ A/cm}^2$  corresponds to  $I_{dc} = 3.5 \text{ mA}$  for the  $L1_0$ -FePt|Cu|Py|Al-O sample, we conclude that the self-induced spin torque of Py and the interface effect at the Cu|Py interface are negligible for the device with the  $L1_0$ -FePt|Cu|Py|Al-O stack.

We confirmed the reproducibility of large  $\alpha_{SAHE}$  by analyzing the modulation of the FMR linewidth using another orthogonal-configuration device (device 2) at different  $\theta_H$ . The FMR spectra and the results of analysis are summarized in the Supplemental Material [22]. The value of  $\alpha_{SAHE}$  was obtained to be  $0.31 \pm 0.05$  for device 2. This large  $\alpha_{SAHE}$  supports the conclusion that the  $L1_0$ -FePt has large SAHE. In addition to the evaluation method based on the modulation of FMR linewidth by the  $I_{dc}$  application, we have tried to do the evaluation of  $\alpha_{SAHE}$  using the FMR line-shape analysis, in which the ratio of the symmetric component of  $V_{dc}$  to the antisymmetric one is used for evaluating  $\alpha_{SAHE}$  and sometimes may give information for the spin-orbit torque [25,26]. However, we found that the line-shape analysis has technical difficulties, and we consider that  $\alpha_{SAHE}$  obtained from line-shape analysis is not reliable for the present devices (see Supplemental Material [22]) because of the existence of inhomogeneous distribution of rf current [27].

### C. Symmetries of SAHE and the other effects

As mentioned in Sec. I, several origins of  $\mathbf{J}_s$ , other than SAHE, have been proposed in the CIP-GMR

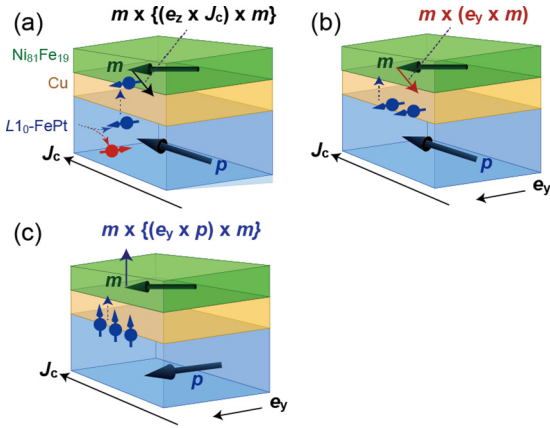


FIG. 5. Schematic illustration of torque of  $M$ -independent SHE ( $\vec{\tau}_{\text{SH}}$ ) and torques due to interface scattering ( $\vec{\tau}_{\text{ISOT},1}$  and  $\vec{\tau}_{\text{ISOT},2}$ ). (a)  $\vec{\tau}_{\text{SH}}$ , (b)  $\vec{\tau}_{\text{ISOT},1}$ , and (c)  $\vec{\tau}_{\text{ISOT},2}$ .

structures. For example, the inverse SHE of Co was reported in Co|Cu|Y<sub>3</sub>Fe<sub>5</sub>O<sub>12</sub> [18], where the spin polarization was geometrically determined and was independent of  $\mathbf{M}$ . Another possible source of  $\mathbf{J}_s$  is the interface scattering effect [19]. Recently, the interface-induced spin-orbit torque was also observed in Py (or CoFeB)|Ti|CoFeB [20].

Symmetries of SAHE,  $M$ -independent SHE, and interface scattering effect are summarized below. The torque due to the SAHE ( $\vec{\tau}_{\text{SAH}}$ ) is expressed as

$$\vec{\tau}_{\text{SAH}} \propto (\mathbf{p} \times \mathbf{J}_c) \cdot \mathbf{e}_z [\mathbf{m} \times (\mathbf{p} \times \mathbf{m})], \quad (5)$$

where  $\mathbf{e}_z$  is a unit vector normal to the film. On the other hand, the torque due to the  $M$ -independent SHE ( $\vec{\tau}_{\text{SH}}$ ) is given by

$$\vec{\tau}_{\text{SH}} \propto \mathbf{m} \times [(\mathbf{e}_z \times \mathbf{J}_c) \times \mathbf{m}], \quad (6)$$

which does not include  $\mathbf{p}$ .  $\mathbf{J}_s$  generated by the interface scattering effect provides two kinds of spin torques. One has the spin polarization identical to that of the  $M$ -independent SHE. The other has the polarization along the direction perpendicular to the film plane, as in the case of the previous work [20]. The torques originating from the interface scattering effect are expressed as

$$\vec{\tau}_{\text{ISOT},1} \propto \mathbf{m} \times [\mathbf{e}_y \times \mathbf{m}], \quad (7)$$

and

$$\vec{\tau}_{\text{ISOT},2} \propto \mathbf{m} \times [(\mathbf{e}_y \times \mathbf{p}) \times \mathbf{m}], \quad (8)$$

where  $\mathbf{e}_y$  is a unit vector orthogonal to  $\mathbf{J}_c$  in the film plane. Figure 5 schematically illustrates the directions of these torques.

From the FMR measurement for the parallel-configuration device, we confirm that such  $M$ -independent SHE, i.e.,  $\vec{\tau}_{\text{SH}}$ , does not exist in our GMR stack. FMR spectra for the parallel-configuration device are shown in Figs. 6(a) and 6(b). Note that SAHE becomes zero in the parallel configuration whereas the  $M$ -independent SHE is finite if it exists. However, no clear  $\theta_H$  dependence of  $d\Delta H_{\text{Res}}/dI_{\text{dc}}$  is seen for the parallel-configuration device as shown in Fig. 6(c). Since our experimental results show no dependence of  $d\Delta H_{\text{Res}}/dI_{\text{dc}}$  on  $\theta_H$  for the parallel-configuration device, we can say that the contributions of  $\vec{\tau}_{\text{SH}}$  and  $\vec{\tau}_{\text{ISOT},1}$  are negligible. Moreover,

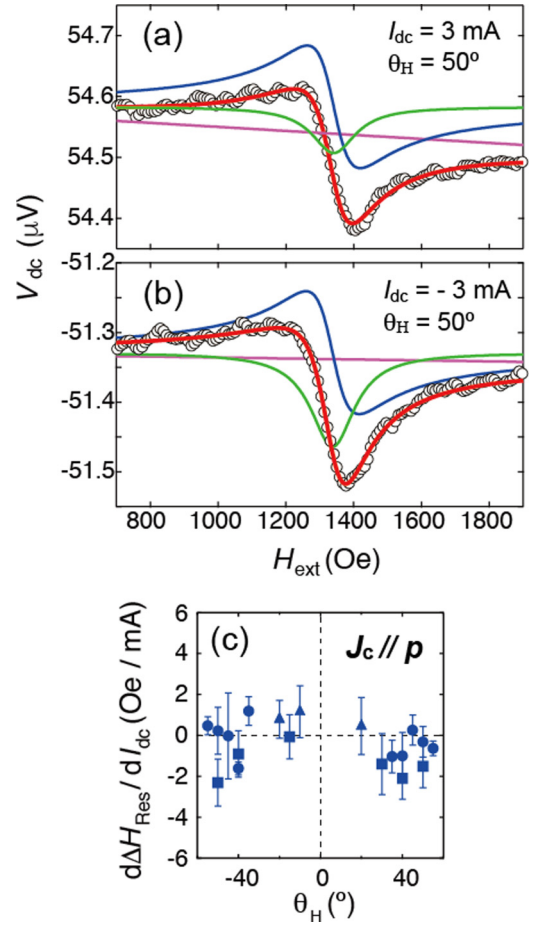


FIG. 6. FMR spectra for parallel-configuration device with  $w = 4 \mu\text{m}$  at (a)  $I_{\text{dc}} = 3 \text{ mA}$  and (b)  $-3 \text{ mA}$ .  $\theta_H$  was set at  $50^\circ$  and  $f_0$  was  $7 \text{ GHz}$ . The experimental data (black open circles) were fitted by a function (red curves) composed of Lorentzian (green curves) and anti-Lorentzian (blue curves) together with the linear background (purple lines). (c)  $d\Delta H_{\text{Res}}/dI_{\text{dc}}$  as a function of  $\theta_H$  for the parallel-configuration device, where the data measured for the different three devices are plotted (denoted by the solid circles, triangles, and squares).

$\vec{\tau}_{\text{ISOT},2}$  is the torque generated by the spin current polarized in the normal direction to the film plane. Thus, this term also does not affect the linewidth modulation. In summary, several phenomena of  $\mathbf{J}_s$  generation reported in the previous works are negligibly small or do not affect our measurement of FMR linewidth, and we can conclude that the modulation of  $\Delta H_{\text{Res}}$  is solely due to the SAHE.

#### D. Magnetization switching by SAHE

Let us move to the magnetization switching experiment. First, the static magnetotransport properties under the  $I_{\text{dc}}$  application are characterized for the orthogonal-configuration device with  $w = 1 \mu\text{m}$ . Minor GMR curves at  $I_{\text{dc}} = 0 \text{ mA}$  and  $\pm 4.8 \text{ mA}$  are shown in Figs. 7(a) and 7(b), respectively, where  $\theta_H$  was set to  $60^\circ$  in order to increase the projection component of  $\mathbf{m}$  to  $\mathbf{p}$ . This projection component is inevitable for deterministic switching. On the other hand, this set value of  $\theta_H$  led to partial (not full) magnetization switching of Py. The

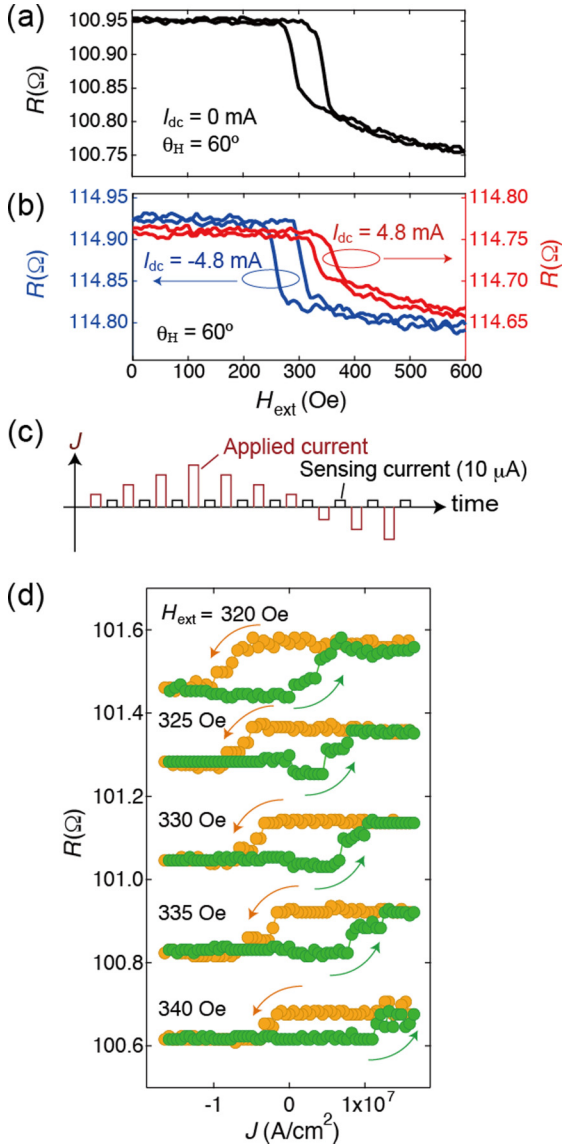


FIG. 7. (a) Minor curves of CIP-GMR for the orthogonal-configuration device with  $w = 1 \mu\text{m}$  at  $\theta_H = 60^\circ$  without  $I_{\text{dc}}$  application and (b) with  $I_{\text{dc}} = 4.8 \text{ mA}$  (red curve) and  $-4.8 \text{ mA}$  (blue curve). (c) Measurement sequence for magnetization switching experiment. First, “applied current” was injected into the device, then  $R$  was measured by small “sensing current” of  $10 \mu\text{A}$ . (d)  $R$  as a function of  $J$  for the orthogonal-configuration device measured at various  $H_{\text{ext}}$ . For clarity, the loops are shifted vertically. The arrows denote the current sweep directions.

remarkable loop shift is observed by applying  $I_{\text{dc}}$ , which is attributable to the SAH torque. The switching experiment was carried out using the measurement sequence shown schematically in Fig. 7(c). Figure 7(d) plots  $R$  as a function of  $J$  for the orthogonal-configuration device. The value of  $R$  is varied from a high-resistance state to a low-resistance state with sweeping  $J$  from positive to negative, and the hysteretic behavior is observed when the sweep direction of  $J$  is reversed, indicating the reversible switching of Py magnetization by applying  $I_{\text{dc}}$ . Also,  $J$  for switching is shifted with  $H_{\text{ext}}$ . The present switching behavior is similar to the conventional switching behavior

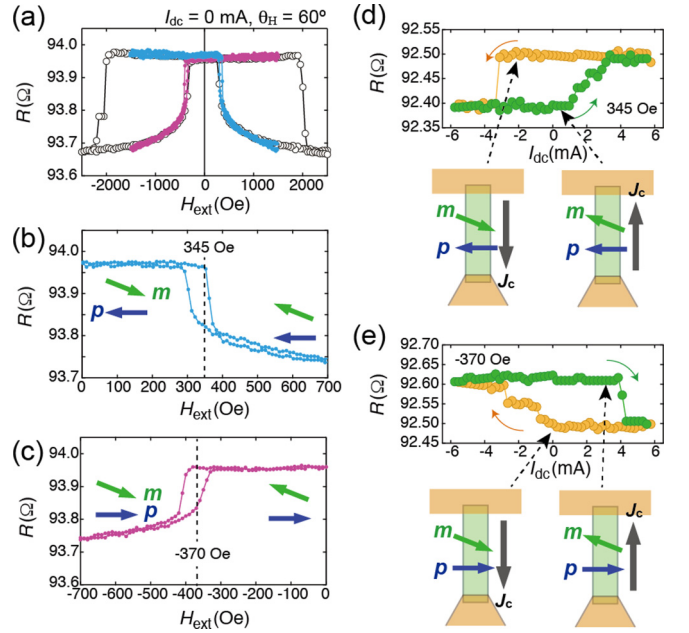


FIG. 8. (a) Full GMR curve at  $I_{\text{dc}} = 0 \text{ mA}$  together with minor loops.  $\theta_H$  was set at  $60^\circ$ . (b,c) Magnified minor loops in which Py and FePt magnetizations,  $\mathbf{m}$  and  $\mathbf{p}$ , were saturated by positive [(b) cyan curve] and negative fields [(c) magenta curve] before starting the measurement. (d)  $R$  as a function of  $I_{\text{dc}}$  at  $H_{\text{ext}} = 345 \text{ Oe}$  and (e)  $-370 \text{ Oe}$ .  $\theta_H$  was set to  $60^\circ$ . Schematic illustrations for explaining the relationship between  $\mathbf{m}$ ,  $\mathbf{p}$ , and  $\mathbf{J}_c$  are also shown.

observed in the spin-orbit torque device using nonmagnetic materials [29–32] and topological insulators [33,34].

A small switching current of  $|J| < 10^7 \text{ A}/\text{cm}^2$  is obtained at  $H_{\text{ext}} = 325 \text{ Oe}$ . Since  $\Delta H = 0$  corresponds to the switching condition, the critical current ( $I_c$ ) for switching is given by

$$I_c = \frac{e\mu_0 w d^{\text{Py}} d^{\text{FePt}} M_s^{\text{Py}} \alpha (H_{\text{XX}} + H_{\text{YY}})}{\hbar C^{\text{FePt}} \alpha_{\text{SAH}} \sin \varphi^{\text{FePt}} \cos(\varphi^{\text{Py}} - \varphi^{\text{FePt}})}, \quad (9)$$

where  $\varphi^{\text{FePt}}$  is the angle of  $\mathbf{p}$  relative to  $\mathbf{J}_c$  and  $\alpha$  is the damping constant of Py. With the assumption of  $\alpha = 0.01$  and  $\varphi^{\text{FePt}} = \varphi^{\text{Py}} = \pi/2$ , the values of switching current and current density are estimated to be  $0.93 \text{ mA}$  and  $3.1 \times 10^6 \text{ A}/\text{cm}^2$ , respectively, by using the experimental value of  $\alpha_{\text{SAHE}}$ . The theoretical value of critical switching current density of  $\sim 3.1 \times 10^6 \text{ A}/\text{cm}^2$  is consistent with the experimental value of  $|J| < 10^7 \text{ A}/\text{cm}^2$ .

Current-induced switching was examined under the condition where  $\mathbf{p}$  has the opposite polarity. Figure 8(a) shows the full GMR curve at  $I_{\text{dc}} = 0 \text{ mA}$  and  $\theta_H = 60^\circ$  together with two minor loops, where  $\mathbf{m}$  and  $\mathbf{p}$  were saturated by a positive magnetic field [Fig. 8(b), cyan curve] and a negative magnetic field [Fig. 8(c), magenta curve] before starting the measurement. Plots of  $R$  as a function of  $I_{\text{dc}}$  at  $H_{\text{ext}} = 345 \text{ Oe}$  and  $-370 \text{ Oe}$  are shown in Figs. 8(d) and 8(e), respectively. The switching condition of  $\mathbf{m}$  is determined by the polarity of  $\mathbf{J}_c$ , and is independent of the sign of  $\mathbf{p}$ . This result is in agreement with the theory of SAHE, and supports the above-stated conclusion that magnetization switching is induced by SAHE.

The contribution of a current-induced Oersted field ( $H_{Oe}$ ) to the magnetization switching is discussed hereafter.  $H_{Oe}$  at the switching current of 1.8 mA was estimated to be  $\sim 10$  Oe, which is smaller than the coercivity of Py ( $\sim 25$  Oe) (see Supplemental Material [22] for details). Therefore, we consider that the SAH torque plays a major role in magnetization switching. In contrast to the orthogonal configuration, magnetization switching was not observed for the parallel-configuration device (see Supplemental Material [22]). This fact also suggests the negligible contribution of SHE and interface scattering effect to magnetization switching.

#### IV. CONCLUSION

We quantitatively evaluated the SAHE in the  $L1_0$ -FePt ferromagnet. From the analysis of linewidth modulation by the  $I_{dc}$  application,  $\alpha_{SAHE}$  was obtained to be  $0.25 \pm 0.03$ . Evaluating the linewidth modulation at the orthogonal and parallel configurations made it possible to discuss the symmetry of SAHE and gave unambiguous evidence that SAHE is the source of  $\mathbf{J}_s$  for the present CIP-GMR device. Thanks to the large  $\alpha_{SAHE}$ , we showed the magnetization switching induced by SAHE. This result is a demonstration of SAHE-induced magnetization switching.

A significant advantage of SAHE is the possibility of zero-field switching of perpendicular  $\mathbf{m}$  by employing an SAHE polarizer with  $\mathbf{p}$  tilted normal to the device plane. Since the  $L1_0$ -FePt (111) with tilted magnetic anisotropy is exploited as a tilted polarizer [35], we believe that the  $L1_0$ -FePt showing large SAHE will be a key material to tackle the essential difficulty the spin-orbit torque devices are confronted with.

#### ACKNOWLEDGMENTS

The authors thank K. Uchida, T. Kikkawa, Y. Miura, K. Masuda, K. Nawa, and S. Takahashi for their valuable comments. I. Narita provided technical support during the structural characterization. This work was supported by the Grant-in-Aid for Scientific Research B (Grant No. JP16H04487), Grant-in-Aid for Challenging Research (Exploratory, Grant No. JP18K19012), Grant-in-Aid for Scientific Research (S) (Grant No. JP18H05246) and Innovative Area “Nano Spin Conversion Science” (Grant No. JP26103005) as well as the Research Grant from the TEPCO Memorial Foundation. The device fabrication was partly carried out at the Cooperative Research and Development Center for Advanced Materials, IMR, Tohoku University.

- 
- [1] M. I. Dyakonov and V. I. Perel, *Phys. Lett. A* **35**, 459 (1971).
- [2] J. E. Hirsch, *Phys. Rev. Lett.* **83**, 1834 (1999).
- [3] Y. K. Kato, R. C. Myers, A. C. Gossard, and D. D. Awschalom, *Science* **306**, 1910 (2004).
- [4] J. Wunderlich, B. Kaestner, J. Sinova, and T. Jungwirth, *Phys. Rev. Lett.* **94**, 047204 (2005).
- [5] A. Hoffman, *IEEE Trans. Magn.* **49**, 5172 (2013).
- [6] J.-C. Tung and G.-Y. Guo, *New J. Phys.* **15**, 033014 (2013).
- [7] B. F. Miao, S. Y. Huang, D. Qu, and C. L. Chien, *Phys. Rev. Lett.* **111**, 066602 (2013).
- [8] S. M. Wu, J. Hoffman, J. E. Pearson, and A. Bhattacharya, *Appl. Phys. Lett.* **105**, 092409 (2014).
- [9] T. Seki, K. Uchida, T. Kikkawa, Z. Qiu, E. Saitoh, and K. Takanashi, *Appl. Phys. Lett.* **107**, 092401 (2015).
- [10] T. Taniguchi, J. Grollier, and M. D. Stiles, *Phys. Rev. Appl.* **3**, 044001 (2015).
- [11] C. Qin, S. Chen, Y. Cai, F. Kandaz, and Y. Ji, *Phys. Rev. B* **96**, 134418 (2017).
- [12] K. S. Das, W. Y. Schoemaker, B. J. van Wees, and I. J. Vera-Marun, *Phys. Rev. B* **96**, 220408(R) (2017).
- [13] S. Iihama, T. Taniguchi, K. Yakushiji, A. Fukushima, Y. Shiota, S. Tsunegi, R. Hiramatsu, S. Yuasa, Y. Suzuki, and H. Kubota, *Nat. Electron.* **1**, 120 (2018).
- [14] J. D. Gibbons, D. MacNeill, R. A. Buhrman, and D. C. Ralph, *Phys. Rev. Appl.* **9**, 064033 (2018).
- [15] J. Cramer, A. Ross, S. Jaiswal, L. Baldrati, R. Lebrun, and M. Kläui, *Phys. Rev. B* **99**, 104414 (2019).
- [16] A. Bose, D. D. Lam, S. Bhuktare, S. Dutta, H. Singh, Y. Jibiki, M. Goto, S. Miwa, and A. A. Tulapurkar, *Phys. Rev. Appl.* **9**, 064026 (2018).
- [17] N. Nagaosa, J. Sinova, S. Onoda, A. H. MacDonald, and N. P. Ong, *Rev. Mod. Phys.* **82**, 1539 (2010).
- [18] D. Tian, Y. Li, D. Qu, S. Y. Huang, X. Jin, and C. L. Chien, *Phys. Rev. B* **94**, 020403(R) (2016).
- [19] V. P. Amin and M. D. Stiles, *Phys. Rev. B* **94**, 104419 (2016).
- [20] S. C. Baek, V. P. Amin, Y. W. Oh, G. Go, S. J. Lee, G. H. Lee, K. J. Kim, M. D. Stiles, B. G. Park, and K. J. Lee, *Nat. Mater.* **17**, 509 (2018).
- [21] K. M. Seemann, Y. Mokrousov, A. Aziz, J. Miguel, F. Kronast, W. Kuch, M. G. Blamire, A. T. Hindmarch, B. J. Hickey, I. Souza, and C. H. Marrows, *Phys. Rev. Lett.* **104**, 076402 (2010).
- [22] See Supplemental Material at <http://link.aps.org/supplemental/10.1103/PhysRevB.100.144427> for derivation of equations, fitting results, magnetic field angular dependence of MR curves and FMR spectra, AHE curve, estimation of current-induced magnetic field, analysis of FMR line-shape, and additional linewidth analysis.
- [23] J. C. Sankey, Y.-T. Cui, J. Z. Sun, J. C. Slonczewski, R. A. Buhrman, and D. C. Ralph, *Nat. Phys.* **4**, 67 (2008).
- [24] C. Wang, Y.-T. Cui, J. Z. Sun, J. A. Katine, R. A. Buhrman, and D. C. Ralph, *Phys. Rev. B* **79**, 224416 (2009).
- [25] L. Liu, T. Moriyama, D. C. Ralph, and R. A. Buhrman, *Phys. Rev. Lett.* **106**, 036601 (2011).
- [26] C. MacNeil, G. M. Stiehl, M. H. D. Guimarães, R. A. Buhrman, J. Park, and D. C. Ralph, *Nat. Phys.* **13**, 300 (2016).
- [27] T. Ikebuchi, T. Moriyama, Y. Shiota, and T. Ono, *Appl. Phys. Express* **11**, 053008 (2018).
- [28] S. Mitani, K. Tsukamoto, T. Seki, T. Shima, and K. Takanashi, *IEEE Trans. Magn.* **41**, 2606 (2005).
- [29] I. M. Miron, K. Garello, G. Gaudin, P.-J. Zermatten, M. Costache, S. Auffret, S. Bandiera, B. Rodmacq, A. Schuhl, and P. Gambardella, *Nature* **476**, 189 (2011).
- [30] L. Liu, C.-F. Pai, Y. Li, H. W. Tseng, D. C. Ralph, and R. A. Buhrman, *Science* **336**, 555 (2012).

- [31] M. Yamanouchi, L. Chen, J. Kim, M. Hayashi, H. Sato, S. Fukami, S. Ikeda, F. Matsukura, and H. Ohno, *Appl. Phys. Lett.* **102**, 212408 (2013).
- [32] S. Fukami, T. Anekawa, C. Zhang, and H. Ohno, *Nat. Nanotechnol.* **11**, 621 (2016).
- [33] Y. Fan, P. Upadhyaya, X. Kou, M. Lang, S. Takei, Z. Wang, J. Tang, L. He, L.-T. Chang, M. Montazeri, G. Yu, W. Jiang, T. Nie, R. N. Schwartz, Y. Tserkovnyak, and K. L. Wang, *Nat. Mater.* **13**, 699 (2014).
- [34] N. H. D. Khang, Y. Ueda, and P. N. Hai, *Nat. Mater.* **17**, 808 (2018).
- [35] C. L. Zha, J. Persson, S. Bonetti, Y. Y. Fang, and J. Åkerman, *Appl. Phys. Lett.* **94**, 163108 (2009).